Experimental Characterization of Non-Directed Indoor Infrared Channels

Joseph M. Kahn, *Member, IEEE,* William J. Krause and Jeffrey B. Carruthers, *Student Member, IEEE*

Abstract— **We have experimentally characterized non-directed indoor channels that use intensity modulation and direct detection of an infrared carrier at a wavelength of 832 nm. At several locations in each of five different rooms, we have studied line-of-sight and diffuse link configurations, with and without shadowing, amounting to a total of approximately 100 different channels. We have measured channel frequency responses over the 2-300 MHz range by using a swept-modulation frequency technique, and from these data, we have computed channel impulse responses, path losses and r.m.s. delay spreads. Using channel impulse responses, we have calculated power penalties induced by multipath intersymbol interference in baseband on-off-keyed links operating at bit rates of 10, 30 and 100 Mb/s, considering unequalized links and those employing zero-forcing decision-feedback equalization. Unshadowed line-of-sight configurations generally have smaller path losses, r.m.s. delay spreads and power penalties than their unshadowed diffuse counterparts. Shadowed line-of-sight configurations, however, generally exhibit larger values of all three parameters than the corresponding shadowed diffuse configurations. We show that among the channels measured here, there is a strong correspondence between channel r.m.s. delay spread and multipath power penalty. Finally, we provide an analysis indicating why non-directed infrared channels using intensity modulation and direct detection do not exhibit multipath fading, and justifying their representation as linear, time-invariant systems.**

I. INTRODUCTION

Non-directed, near-infrared radiation [1-5] is an attractive transmission medium for wireless indoor local-area networks. Advantages offered by infrared over radio include the availability of a virtually unlimited, unregulated spectrum, and the fact that infrared radiation does not pass through walls or other opaque barriers. Since it is possible to operate at least one infrared link in every room of a building without interference, the potential capacity of an infrared-based in-building network is extremely high. When an infrared link employs intensity modulation with direct detection (IM/DD), the short carrier wavelength and large, square-law detector lead to efficient spatial diversity that prevents multipath fading. Drawbacks of infrared systems include the existence in many environments of an intense infrared ambient, which induces receiver shot noise. As a result, infrared links must often employ relatively high transmit power levels and operate over a comparatively limited range.

Paper approved by Reinaldo A. Valenzuela, the Editor for Transmission Systems of the IEEE Communications Society. Manuscript received September 13, 1993; revised October 20, 1994. This research was supported by the AT&T Foundation and by National Science Foundation PYI Award ECS-9157089.

The authors are with the Department of Electrical Engineering and Computer Sciences, University of California at Berkeley, CA 94720 USA.

IEEE Log Number 9411627.

0090-6778/95$4.00

While infrared links are immune to multipath fading, the existence of multiple propagation paths does lead to temporal dispersion [5,7], potentially causing intersymbol interference (ISI) in digital links with signaling rates greater than about 10 Mbaud. In this paper, we report on experimental characterization of the multipath dispersion of approximately 100 infrared channels, and using measured channel responses, we quantify the power penalties that ISI induces in baseband on-off-keyed (OOK) links. The remainder of this paper is organized as follows. Section II, in conjunction with the Appendix, describes the modeling of non-directed infrared channels as linear, time-invariant (LTI) systems. In Section III, we describe our experimental measurement technique. Measured channel characteristics are presented in Section IV. Section V evaluates the performance of baseband OOK links over the measured channels, and conclusions are presented in Section VI.

II. NON-DIRECTED INFRARED CHANNELS

Non-directed infrared links may be classified as *line-of-sight* (LOS), which depend upon the existence of an unobstructed path between transmitter and receiver; and *diffuse*, which alleviate the need for a LOS path by relying on reflections from a large diffuse reflector, such as a ceiling. In both LOS and diffuse links, the infrared channel, like a multipath radio channel, exhibits substantial variations of received power on a distance scale of the order of a wavelength. In IM/DD infrared systems, which typically use a square-law detector much larger than the wavelength, such fluctuations are averaged out effectively, so that these links are not susceptible to multipath fading.

The existence of multiple propagation paths does lead to temporal dispersion. The channel temporal response is fixed for a given configuration of source, reflectors and receiver, and changes in this response are observable only if the configuration is changed on a distance scale of at least $c\Delta t$, where c is the speed of light and Δt is the measurement temporal resolution. In the Appendix, we provide analysis showing why IM/DD infrared channels are immune to multipath fading, and justifying their representation as LTI systems. While mobile transmitters, receivers, and reflectors will result in a time-varying channel, we will ignore this effect because in most cases the channel will vary significantly only on the time scale of many symbol periods.

Infrared links are often operated in the presence of intense ambient light, which leads to a high-intensity shot noise that can be represented by a white, nearly Gaussian process [6]. In most applications, this shot noise limits the signal-to-noise ratio of a well-designed infrared receiver

[1,4,5]. The characteristics of IM/DD infrared channels may be summarized in a simple form:

$$Y(t) = X(t) \otimes h(t) + N(t). \quad (1)$$

The received photocurrent $Y(t)$ is the convolution of the transmitted optical power $X(t)$ with a channel impulse response $h(t)$ (fixed for a given configuration of transmitter, receiver and intervening reflectors), plus an additive noise $N(t)$, which is usually modeled as white and Gaussian.

Barry *et al.* have previously reported a method [7] to simulate the multipath impulse response $h(t)$ for an arbitrary configuration of transmitter and receiver in an arbitrary room that is comprised of diffuse reflectors, and including contributions to $h(t)$ from light that has undergone multiple bounces. This simulation methodology yields multipath responses that are in reasonable agreement with experimentally measured responses.

III. MEASUREMENT TECHNIQUE

Several different techniques commonly used in measurement of radio channels [8] can be adapted to characterization of non-directed infrared channels. The short-pulse technique, which uses a short transmitted pulse to directly probe the channel impulse response, is straightforward to implement. In view of transmitter peak-power limitations, however, the use of such a low-duty cycle waveform may require long measurement times for achievement of high signal-to-noise (SNR) ratio. Measurement time can be reduced through use of pseudo-random noise cross-correlation techniques. In such techniques, one transmits a pseudo-random binary sequence (PRBS) having approximately 50% duty cycle, and obtains an approximation to the channel impulse response by cross-correlation of the received signal with the transmitted PRBS. Similar measurement efficiency can be achieved using the CW swept-frequency technique, which uses a constant-amplitude, swept-frequency sinusoid to probe the channel. The received signal is multiplied by the transmitted signal and by a 90° phase-shifted version of the transmitted signal. These product signals are low-pass filtered and normalized to the transmitted signal amplitude, yielding estimates of the real and imaginary parts of the channel frequency response, which is the Fourier transform of the channel impulse response. We have chosen to employ this technique for our measurements, as it can be implemented easily and accurately using a vector network analyzer.

A. Measurement System

The block diagram of our measurement system is shown in Fig. 1. The transmitter contains a 832-nm laser diode of 100-mW nominal output power (Spectra Diode Labs SDL-5311) that is placed on a microstrip line containing a 47-Ω impedance-matching resistor and bias tee to permit IM over a bandwidth from 300 kHz to at least 1 GHz. The laser emission is directed into the polished interior of a $10 \times 10 \times 15$ cm^3 aluminum box through a hole in the center of a 10×15 cm^2 face, and is then emitted through a 3-mm-thick, translucent, white plexiglas diffuser attached along

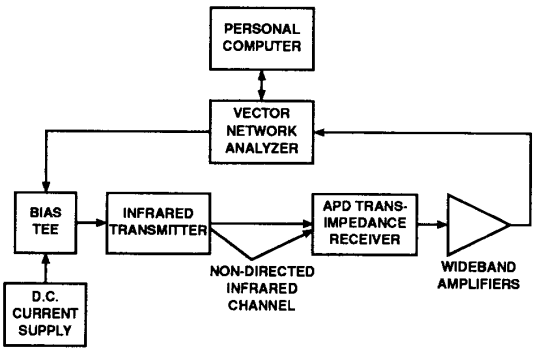

Fig. 1. Block diagram of measurement system. The transmitter emits a Lambertian radiation pattern, has a wavelength of 832 nm and peak power of 95 mW, and is intensity-modulated by a swept-frequency sinusoid from the network analyzer. The receiver, which uses a 5 mm × 5 mm silicon avalanche photodiode, has a 3-dB cutoff frequency of 150 MHz and an acceptance half-angle of about 70°. The overall system achieves a useful measurement range from near d.c. to 300 MHz.

the opposing face. While only approximately 50% of the incident light passes through the diffuser, multiple reflections within the box result in an overall efficiency of about 70%. The transmitter emits an eye-safe, Lambertian radiation pattern (power per unit solid angle proportional to the cosine of the angle with respect to transmitter surface normal). When driven by the network analyzer, the transmitter emission is sinusoidally intensity-modulated with 95-mW peak output power and nearly 100% modulation depth.

The receiver includes a packaged, 5×5 mm^2 silicon avalanche photodiode (APD) having an acceptance half-angle of about 70° and a capacitance of about 30 pF (EG&G C30626E). The APD is coupled to a transimpedance preamplifier employing a 250-Ω feedback resistor and a wideband operational amplifier (ComLinear CLC-400). The receiver exhibits a single-pole response from near d.c. to about 400 MHz, with a 3-dB cutoff frequency of 150 MHz. The receiver output is amplified by several d.c.-to-500 MHz video amplifiers (ComLinear CLC-100).

Frequency-response measurements are performed using a 300 kHz-to-3 GHz vector network analyzer (HP8753A) coupled to a personal computer. The measured frequency response is recorded at 2-MHz intervals between 2 MHz and 400 MHz and stored in complex format; the response at d.c. is taken to be a real number extrapolated from the magnitude of the response at nonzero frequencies. To maximize the SNR, measurements are performed with an intermediate-frequency bandwidth of 10 Hz and a sweep time of 20 s. Channel measurements are calibrated using a 1-m-long LOS reference channel that has known loss and negligible temporal dispersion. After normalization, the measurement system achieves a useful measurement bandwidth from near d.c. to about 300 MHz, limited at high frequencies by direct pickup of the laser electrical drive signal.

B. Definition of Measured Quantities

We present measurements in terms of a *channel frequency response* $H(f)$, scaled so that $H(0)$ represents the fraction of the transmitted average optical power that is received by a 1-cm^2 detector having an acceptance half-angle of 70°. We define the *channel path loss* as the reciprocal of $H(0)$.

We obtain the *channel impulse response* $h(t)$ by inverse Fourier transformation of $H(f)$, using a Hamming window that provides 3-dB attenuation at 125 MHz and infinite attenuation at 300 MHz. The inverse Fourier transform of this window is a pulse having a full width of 3 ns at half-maximum, and of 7 ns at its base. In order to compare the temporal dispersion of different channels, we define the *channel r.m.s. delay spread* D, which is calculated from the impulse response according to:

$$D = \left[\frac{\int (t-\mu)^2 h^2(t)dt}{\int h^2(t)dt} \right]^{1/2}, \tag{2}$$

where the mean delay μ is given by:

$$\mu = \frac{\int t h^2(t)dt}{\int h^2(t)dt}, \tag{3}$$

and the limits of integration in (2) and (3) extend over all time. We emphasize that since $h(t)$ is fixed for a given configuration, so is the r.m.s. delay spread. It should be noted that our use of the 300-MHz Hamming window in calculating $h(t)$ leads to a 1.3-ns floor in computed values of the r.m.s. delay spread.

IV. MEASURED CHANNEL CHARACTERISTICS

A. Description of Rooms and Configurations

Channel measurements have been performed in five rooms, which are pictured in Figs. 2(a), 3(a) and 4(a-c). Rooms A and C are empty conference rooms, while Rooms B, D and E are offices containing desks and other office furniture. We have characterized the diffuse reflectivity of the surfaces in Room A; these measurements neglect any specularly reflected components and thus may not fully characterize the surface reflections. In this room, the floor and one wall are covered in gray carpet having 9% diffuse reflectivity. Two walls are covered with textured acoustic tiles having 30% diffuse reflectivity, while the fourth wall, which is painted, has a diffuse reflectivity of 56%. The ceiling is covered by vinyl-coated tiles having 65% diffuse reflectivity; these tiles exhibit substantial additional specular reflections that have not been quantified. Rooms B-E have walls with diffuse reflectivities ranging from 10% to 90%, ceilings with diffuse reflectivities between 65% and 90%, and floors with diffuse reflectivities of the order of 10% (some linoleum floors also exhibit a strong specular component).

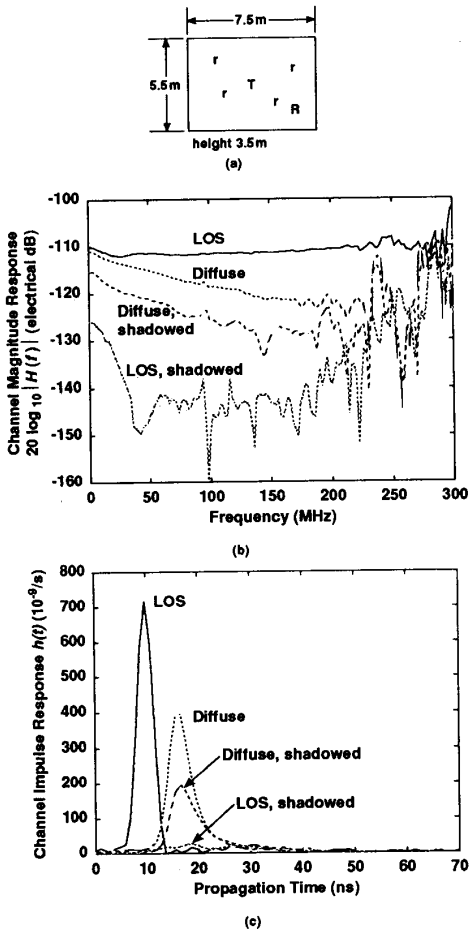

Fig. 2. Room A. (a) Top view of room (see text for additional description). The transmitter, at location T, is either placed at ceiling and pointed straight down (LOS configuration) or placed 1 m above floor and pointed straight up (diffuse configuration). For measurements shown here, receiver is located at position R and pointed straight up; additional measurements have been performed with receiver at locations r. (b) Channel magnitude response $|H(f)|$, scaled so that $H(0)$ represents the fraction of the transmitted optical power that is received by a 1-cm^2 detector having an acceptance half-angle of 70°. (c) Channel impulse response, obtained by inverse Fourier transformation of $H(f)$ using a 300-MHz Hamming window.

During all measurements, the receiver is pointed straight up and placed 0.76 m above the floor at the locations denoted either "R" or "r" in Figs. 2, 3 and 4, while the transmitter is placed at the locations denoted "T" in those figures. For *LOS* configurations, the transmitter is placed 0.15 m below ceiling height and pointed straight down, while for *diffuse* configurations, it is placed 1.2 m above the floor and pointed straight up. The *shadowed LOS* configurations are formed by using the LOS transmitter and having a person stand next to the receiver such that the main signal path is obstructed. To form *shadowed diffuse* configurations, we use the diffuse transmitter and have the

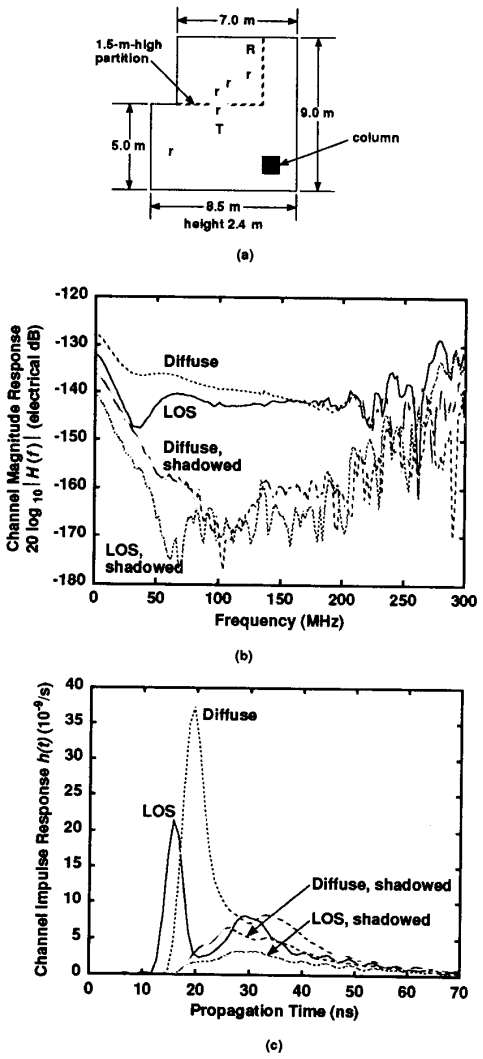

Fig. 3. Room B. (a) Top view of room. For measurements shown here, receiver is located at position R and pointed straight up; additional measurements have been performed with receiver at locations r. (b) Channel magnitude response. (c) Channel impulse response.

person stand in that same location.

B. Frequency and Impulse Response

Figs. 2(b) and 3(b) display the magnitudes of the frequency responses of channels measured in Rooms A and B. Note that these curves assume a ragged appearance when the channel magnitude response approaches or falls below the measurement system noise floor. The corresponding impulse responses are presented in Figs. 2(c) and 3(c). Channel responses measured at all positions in all rooms exhibit qualitative similarity to these.

The unshadowed LOS impulse responses are dominated by a short initial pulse, whose measured width is broadened by our use of the 300-MHz Hamming window. The strongest distinct reflections typically arrive 15 to 20 ns after the initial pulse, usually arising from primary reflections off the far wall and secondary reflections off the ceiling (transmitter to floor to ceiling to receiver). Dominance of the short initial pulse leads to magnitude responses that are flat at high frequencies. At lower frequencies, the magnitude responses exhibit ripples that are most pronounced for channels exhibiting relatively strong reflected components. The d.c. gain of unshadowed LOS channels (and of all channels) is enhanced over that at high frequencies, because it includes the contribution due to the entire duration of the impulse response. In LOS channels (and in all channels), the impulse response may contain significant energy as long as 70 ns after its initial nonzero excursion.

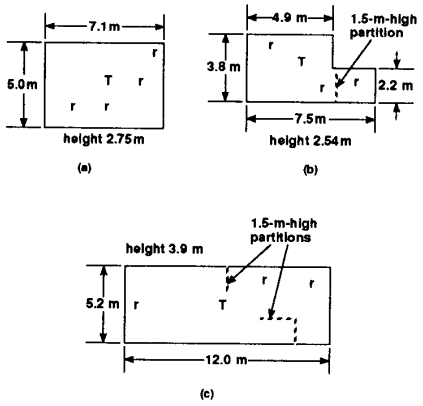

Fig. 4. Top views of additional rooms. (a) Room C. (b) Room D. (c) Room E.

The unshadowed diffuse impulse responses exhibit a significantly wider initial pulse, which has a width of about 12 ns at 10% height, corresponding to the existence of a continuum of different path lengths between illuminated portions of the ceiling and the receiver. This continuous distribution of path delays leads to a monotonic decrease in the channel magnitude response at high frequencies. In diffuse impulse responses, secondary reflections tend to blend directly into the tail of the initial broad pulse, rather than appearing as distinctly separate arrivals.

The shadowed channels exhibit characteristics that are slightly less predictable than the unshadowed channels. The shadowed LOS impulse response typically resembles the corresponding unshadowed response with the dominant initial pulse removed, since only the primary and secondary reflection paths remain. Primary reflections from the near wall combine with primary reflections from the far wall and with secondary reflections to form a multi-humped impulse response. On close inspection, it becomes clear that the near-wall primary reflections are also present in unshadowed LOS channels, but are obscured there by the end of the dominant initial pulse. We observe that in LOS configurations, shadowing greatly decreases the channel d.c. gain, typically by 10-15 dB, and significantly degrades the

channel frequency and impulse responses.

Diffuse configurations are far less vulnerable to shadowing than their LOS counterparts, because in diffuse configurations there exist many possible propagation paths between the illuminated ceiling area and the receiver. In diffuse configurations, shadowing decreases the channel d.c. gain by about 3-8 dB. Typically, it produces a slight broadening of the impulse response, and a slight increase in the rate of falloff of the magnitude response with increasing frequency.

We have computed the frequency-dependent group delay of infrared channels, by differentiation of the frequency-dependent phase response. At high frequency, these group-delay responses are constant, with a value equal to the propagation delay of the dominant component of the impulse response. Excepting frequency ranges where the magnitude response exhibits sharp notches, the group delays vary slowly with frequency, and show a total peak-to-peak excursion not exceeding 10 ns. Measured group delays are largest at d.c., due to the contribution from the long tail of the impulse response.

C. Path Loss

Fig. 5 displays the path loss versus horizontal separation between transmitter and receiver for unshadowed LOS and diffuse channels in Room B. LOS path losses range from 48 dB at zero horizontal separation to 66 dB at 4.7-m separation. Considering a Lambertian radiated pattern, neglecting the contribution of indirect propagation paths, and assuming for simplicity a detector field-of-view half-angle of 90°, the loss of the unshadowed LOS channel can be computed approximately from the formula [1]:

$$\text{LOS path loss (optical dB)} = -10\log_{10}\left[\frac{A_R}{\pi}\frac{h^2}{(h^2+d^2)^2}\right]. \quad (4)$$

Here, h is the vertical separation between transmitter and receiver, d is their horizontal separation, and we must choose a detector area $A_R = 1$ cm^2 to conform to our definition of path loss. The path loss calculated using (4), which is indicated by the solid curve in Fig. 5, agrees well with losses measured for small horizontal separation, where the LOS path dominates. While (4) follows the observed trend, it overestimates path loss by about 2-3 dB for large horizontal separations, where neglected indirect propagation paths contribute most significantly. It is important to note that the observed rapid increase of path loss with horizontal separation is an artifact of using a sub-optimal, Lambertian radiation pattern, and an optimally designed source distribution would yield a path loss independent of horizontal separation [5].

For the unshadowed diffuse configuration, path losses measured in Room B range from 53 dB at zero transmitter-receiver separation, which is larger than for the LOS configuration, to 64 dB at 4.7-m separation, which is smaller than for LOS. The path loss of an unshadowed diffuse configuration can be estimated using the expression [2]:

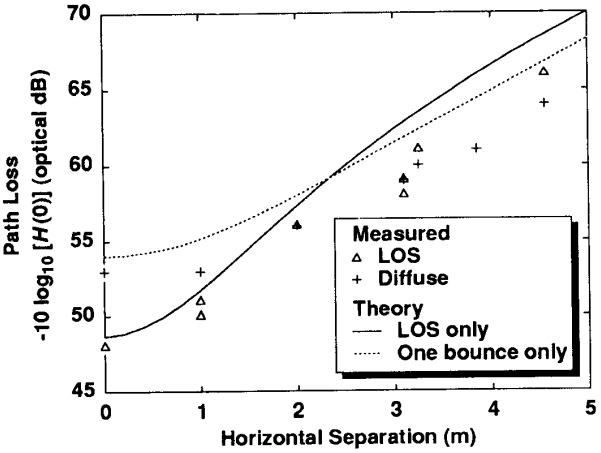

Fig. 5. Path loss versus horizontal separation between transmitter and receiver in Room B. Path loss is defined as the ratio of the transmitted average optical power to the average optical power received by a 1-cm^2 detector having an acceptance half-angle of 70°. Symbols represent measurements, while curves represent simplified theory taking account of dominant propagation paths only.

$$\text{diffuse path loss (optical dB)} = -10\log_{10}\left[\frac{\rho A_R h_1^2 h_2^2}{\pi^2} \times \iint_{ceiling} \frac{dx\,dy}{(h_1^2+x^2+y^2)^2\left[h_2^2+(x-x_2)^2+(y-y_2)^2\right]^2}\right]. \quad (5)$$

The expression (5) assumes a detector field-of-view half-angle of 90° and a Lambertian source, and considers only contributions from the initial bounce off of the ceiling, which is assumed to be a Lambertian reflector of reflectivity ρ. The transmitter and receiver are located, respectively, at coordinates $(0,0)$ and (x_2, y_2) in the horizontal (x, y) plane, and h_1 and h_2 represent the transmitter-ceiling and receiver-ceiling vertical separations, respectively. Using the measured ceiling reflectivity of $\rho = 80\%$, taking $A_R = 1$ cm^2 to conform to our definition of path loss, and considering an infinite ceiling for simplicity, we integrated (5) numerically to obtain the dotted curve of Fig. 5. This curve follows well the experimentally observed trend, but it overestimates the path loss by as much as 3 dB, especially at large horizontal separations, where the effect of neglected higher-order reflections is relatively important.

The path loss versus horizontal separation for all measured channels is displayed in Fig. 6. For a given horizontal separation, the unshadowed LOS configuration generally yields the lowest path loss, and the path loss of the corresponding unshadowed diffuse configuration is typically 1-3 dB higher. In the presence of shadowing, however, LOS configurations exhibit typically a 7-10 dB increase in path loss, while in the diffuse case, the corresponding increase is about 2-5 dB. As a result, shadowed diffuse configurations typically yields path losses that are 2-5 dB smaller than the corresponding shadowed LOS configurations, clearly indi-

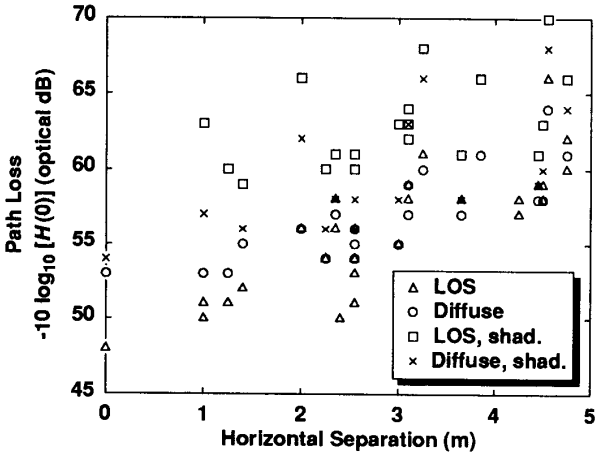

Fig. 6. Path loss versus horizontal separation between transmitter and receiver measured in Rooms A-E.

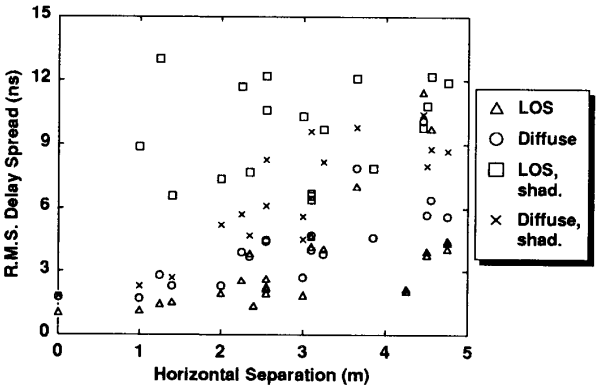

Fig. 7. Root-mean-square delay spread, defined by (2), versus horizontal separation between transmitter and receiver, measured in Rooms A-E.

cating the robustness of an extended, diffuse source.

D. R.M.S. Delay Spread

Fig. 7 presents the r.m.s. delay spread versus horizontal separation for all measured channels, computed using (2). We recall that since the impulse response is fixed for a given configuration of transmitter, receiver and objects in the room, so is the delay spread. In the absence of shadowing, LOS channels, whose impulse response is dominated by a short initial pulse, generally yield the smallest delay spreads, ranging from 1.3 ns (limited by the 300-MHz Hamming window) to about 12 ns. Unshadowed diffuse channels exhibit delay spreads that lie in the same range, but which are systematically slightly larger, due to the finite temporal spread of the dominant reflection from the ceiling. Shadowing increases the delay spread of both LOS and diffuse channels but, as might be expected, the increase is relatively modest for the latter channels. Shadowed LOS channels consistently exhibit the largest delay spreads, typically between 7 and 13 ns.

V. PERFORMANCE OF BASEBAND ON-OFF KEYING

A. Intersymbol Interference Penalty without Equalization

Our performance analysis of unequalized OOK follows that of [7]. Symbols $a_k \in \{0, 1\}$ are passed through a transmit filter with impulse response $Ab(t)$ at a bit rate of $1/T$, where A is proportional to the average optical power of the transmitter. After passage through the channel with impulse response $h(t)$, the signal is processed by the receiver filter $g(t)$ and sampled. The receiver makes decisions based on the samples:

$$y_k = Aa_k \otimes h_k + n_k. \tag{6}$$

The discrete-time link impulse response h_k is given by:

$$h_k = b(t) \otimes h(t) \otimes g(t)|_{t=kT}, \tag{7}$$

with the normalization $\sum_k h_k = 1$; it is assumed that the sampling times are shifted to maximize the zero-sample h_0. The noise samples n_k, which have zero mean and variance σ^2, are given by:

$$n_k = n(t) \otimes g(t)|_{t=kT}. \tag{8}$$

In the absence of ISI, the bit-error rate (BER) is given by $BER = Q(A/2\sigma)$. When ISI is present, the BER is obtained by averaging over all possible M-bit sequences $\mathbf{a}$, where M is the length of the impulse-response tail $(1 - \delta_k)h_k$, assumed to be finite:

$$BER = \frac{1}{2^M} \sum_{\mathbf{a}} Q\left(\frac{A}{2\sigma}\left(1 - 2\sum_{i \neq k} a_i h_{k-i}\right)\right). \tag{9}$$

We define the multipath power penalty as the increase in optical power required to maintain the same BER as a link transmitting over an ideal, nondispersive channel having the same path loss, and using a matched receiver filter. At a BER of BER_0, it is given by:

$$\text{unequalized power penalty (optical dB)} = 10 \log_{10}\left[\frac{\frac{A}{2\sigma}\text{required for} BER_0}{Q^{-1}(BER_0)}\right]. \tag{10}$$

We note that if $h_0 < 1/2$ then the eye pattern is closed due to ISI, and is not possible to reach an arbitrarily low BER.

We have used (10) to calculate multipath power penalties for unequalized reception of OOK over all experimentally measured channels. We assume a rectangular transmitted pulse of duration T, a five-pole Bessel receiver filter of 3-dB cutoff frequency $0.6/T$, and $BER_0 = 10^{-9}$. At a bit rate of 10 Mb/s, power penalties are modest, lying in the range of 0.3 to 1.0 dB. Fig. 8 presents power penalties for bit rates of 30 and 100 Mb/s. At 30 Mb/s, power penalties for unshadowed LOS and diffuse channels do not exceed 4.0 and 4.2 dB, respectively. When shadowing occurs, LOS channels incur power penalties as high as 5.3 dB, while those for

diffuse channels remain below 4.3 dB. These unequalized power penalties, though substantial, may be acceptable for some applications. At a bit rate of 100 Mb/s, however, very large or infinite power penalties are incurred by links using all four configurations, suggesting that unequalized OOK is not practical at this bit rate.

At low values of BER, the degradation due to multipath ISI is dominated by the degradation of the worst-case bit sequences, which consist of a single one bit preceded and followed by long strings of zeros, and the complement of that sequence. In this case, the expression (9) reduces to:

$$BER \approx \frac{1}{2^M} Q\left(\frac{A}{2\sigma}(2h_0 - 1)\right), \tag{11}$$

and the power penalty becomes:

$$\text{unequalized power penalty, low BER (optical dB)} = 10\log_{10}\left[\frac{Q^{-1}(2^M BER_0)}{(2h_0 - 1)Q^{-1}(BER_0)}\right]. \tag{12}$$

We note that the low-BER asymptotic penalty (12) depends on h_k only through h_0 and M; furthermore, when $h_0 = 1/2$, this expression yields an infinite penalty, as expected. In Fig. 9, the penalty computed using (12) is compared to penalties computed using the exact formula (10) for 100-Mb/s, unequalized OOK at 10^{-9} BER for all measured channels that yield finite penalties. It is seen that (12) provides a very good estimate of the exact power penalty.

B. ISI Penalty with Decision-Feedback Equalization

Adaptive decision-feedback equalization (DFE) is a practical, though sub-optimal, means to overcome ISI [9]. In general, the best-performing DFE is one that minimizes the mean-square error (MSE) at the slicer input. It has been shown [10] that for typical infrared channels at low BER (BER $\leq 10^{-6}$), virtually the same performance can be achieved by a zero-forcing DFE (ZF-DFE), which completely cancels ISI at the slicer input. For a receiver employing a perfectly adapted ZF-DFE of unconstrained complexity, the electrical SNR penalty due to ISI is equal to the ratio of slicer MSE for the ZF-DFE to the MSE for matched-filter reception of an isolated pulse [9]. The optical power penalty is given by:

$$\text{ZF-DFE power penalty (optical dB)} = -5\log_{10}\left[GM\left(\frac{|H_{eq}(e^{j\omega t})|^2}{S_{G,eq}(e^{j\omega t})}\right)\right]. \tag{13}$$

Here, $H_{eq}(e^{j\omega t})$ and $S_{G,eq}(e^{j\omega t})$ are the discrete-time Fourier transforms of the sequences h_k and $g(t) \otimes g^*(-t)|_{t=kT}$, respectively, and GM denotes the geometric mean over the interval $\omega \in [-\pi/T, \pi/T)$.

We have used (13) to evaluate multipath power penalties for OOK links with ZF-DFE over all measured channels. All link parameters are the same as those described above for unequalized reception, except that the five-pole Bessel receiver filter is taken to have a 3-dB cutoff frequency of 0.45/T, which generally yields the best performance. We note that these penalties are independent of BER. Fig. 10 presents power penalties for bit rates of 30 and 100 Mb/s. At 30 Mb/s, power penalties for most channels are less than 2 dB, and the highest penalties, for shadowed LOS channels, are 2.3 dB. At 100 Mb/s, penalties for unshadowed LOS and diffuse channels are less than 6.7 and 5.7 dB, respectively, while those for shadowed LOS and diffuse channels do not exceed 9.1 and 7.1 dB, respectively. It should be emphasized that for most choices of transmitter and receiver location, when shadowing occurs, diffuse configurations yield penalties that are 2 to 5 dB smaller than their LOS counterparts. Calculated ISI penalties indicate that OOK with ZF-DFE is very feasible for 30 Mb/s, and, if a diffuse configuration is employed, may be practical at 100 Mb/s as well. Numerical simulations [10,11] of 100 Mb/s OOK with constrained-complexity DFEs have shown that have shown that little degradation is caused by limiting the forward and reverse filters to three $T/2$-spaced taps and five T-spaced taps, respectively, nor by employing four-bit quantization of tap weights. Adaptation to a training sequence using the least-mean-squares algorithm

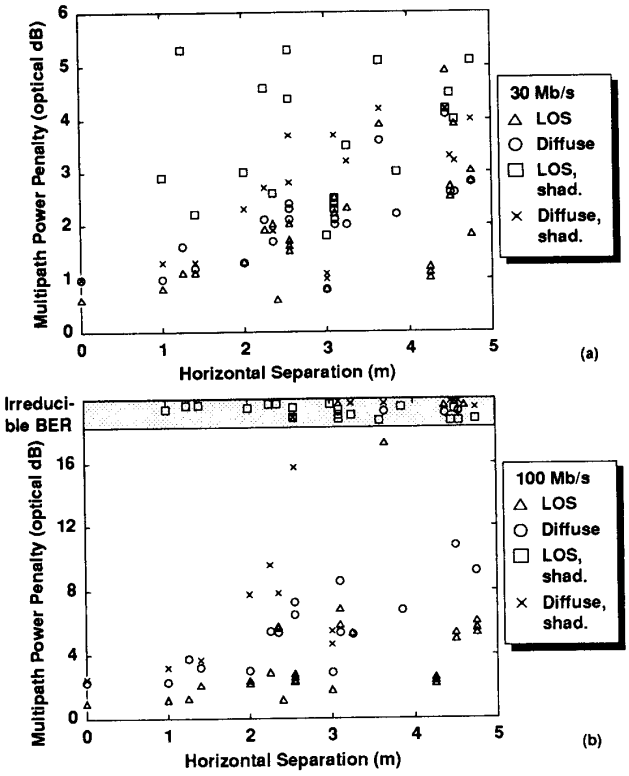

Fig. 8. Unequalized baseband on-off keying: optical power penalty caused by intersymbol interference. Transmitter employs rectangular pulses of duration T, receiver employs five-pole Bessel filter with 3-dB cutoff of $0.6/T$, and BER is 10^{-9}. (a) 30 Mb/s. (b) 100 Mb/s. In region of irreducible bit-error rate (infinite penalty), the different symbols have been vertically separated to enhance visibility.

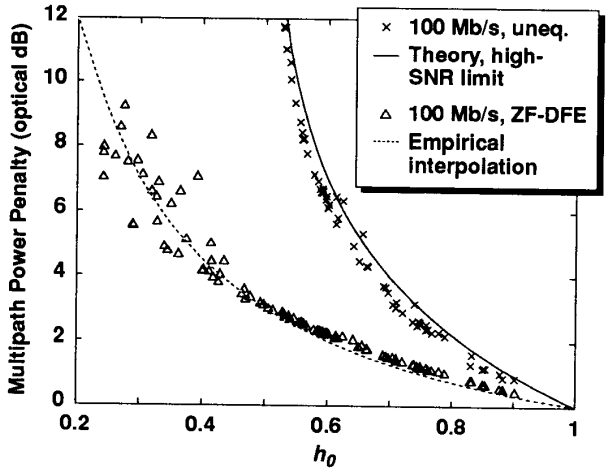

Fig. 9. Baseband on-off keying at 100 Mb/s, unequalized and with zero-forcing decision-feedback equalization: optical power penalty caused by intersymbol interference versus h_0, the zero-sample of the discrete-time impulse response given by (7). Symbols represent penalties calculated from all measured channels that yield finite penalties, including all four types of link configurations, using same parameters as in Figs. 8 and 10. Solid curve represents theoretical unequalized power penalty in high-SNR limit (10), while dotted curve represents empirical interpolation formula (14).

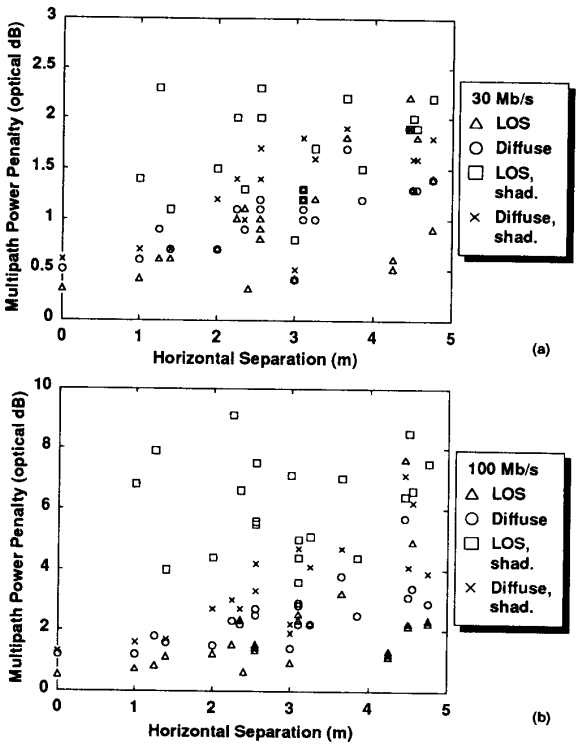

Fig. 10. Baseband on-off keying with zero-forcing decision-feedback equalization: optical power penalty caused by intersymbol interference. Transmitter employs rectangular pulses of duration T and receiver employs five-pole Bessel filter with 3-dB cutoff of $0.45/T$. (a) 30 Mb/s. (b) 100 Mb/s.

was found to occur within about 200 bits, i.e., about 2 μs.

Unlike the case of unequalized OOK, there is no simple relationship between the ISI penalty for equalized OOK and h_0, the zero-sample of h_k, even in the high-SNR limit. Nonetheless, we have found that the trend of these power penalties is described by the simple expression:

$$\text{ZF-DFE power penalty(optical dB)} \approx 3\left(\frac{1}{h_0} - 1\right). \quad (14)$$

We note that when $h_0 = 1$, (14) gives the correct penalty of 0 dB, while when $h_0 = 1/2$, it yields 3 dB, which is the exact penalty [6] for a two-tap discrete-time impulse response with $h_0 = h_1 = 1/2$. In Fig. 9, exact power penalties computed for a bit rate of 100 Mb/s over channels of all four types are compared to (14). It is seen that (14) describes the systematic dependence of the power penalty upon h_0 for all values of h_0, and that it yields a very good estimate of the exact penalty for $h_0 \geq 0.45$.

C. Relationship Between Channel Delay Spread and ISI Penalty

As illustrated in Fig. 11, there is a systematic relationship between multipath power penalties for baseband OOK and the normalized delay spread, which is the channel r.m.s. delay spread (2) divided by the bit duration T. For channels of all four types having normalized delay spreads less than 0.5, the power penalty for unequalized OOK at 30 and 100 Mb/s is approximated by the least-squares linear expression:

$$\text{unequalized power penalty (optical dB)} \approx 13.2(\text{normalized delay spread}) + 0.2, \quad (15)$$

with 95% of the penalties lying within 1.2 dB of (15). For the same bit rates and over the same range of normalized delay spreads, the ZF-DFE penalty for channels of all types is fitted by:

$$\text{ZF-DFE power penalty (optical dB)} \approx 4.7(\text{normalized delay spread}) + 0.4, \quad (16)$$

with a 95% confidence interval of 0.4 dB. The systematic relationship between power penalty and delay spread is somewhat surprising. For a given link design and bit rate, the ISI power penalties are completely determined by the discrete-time impulse response h_k, and two different h_k that are derived from continuous-time channels having very different delay spreads may give rise to precisely the same ISI penalties. The observed close correspondence between power penalty and delay spread implies that there exist some underlying similarities between all of the measured channel responses, so that for purposes of calculating ISI penalties, channels of all four types may be roughly de-

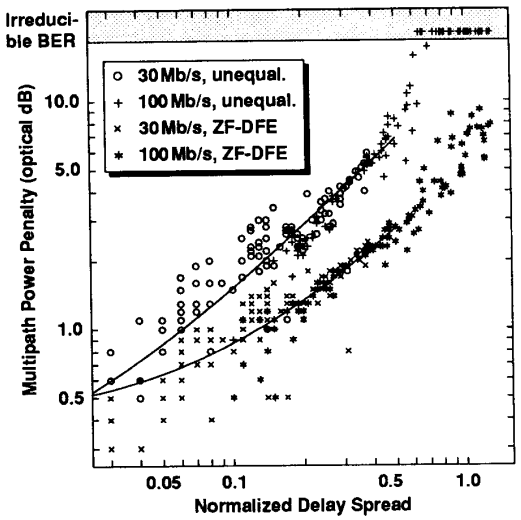

Fig. 11. Baseband on-off keying at 30 and 100 Mb/s, unequalized and with zero-forcing decision-feedback equalization: optical power penalty caused by intersymbol interference versus normalized delay spread [r.m.s. delay spread (2) divided by bit duration]. Symbols represent penalties calculated from all measured channels, including all four types of link configurations, using same parameters as in Figs. 8 and 10. Curves represent a least-squares linear fit of the power penalty (in dB) to the normalized delay spread for normalized delay spreads less than 0.5.

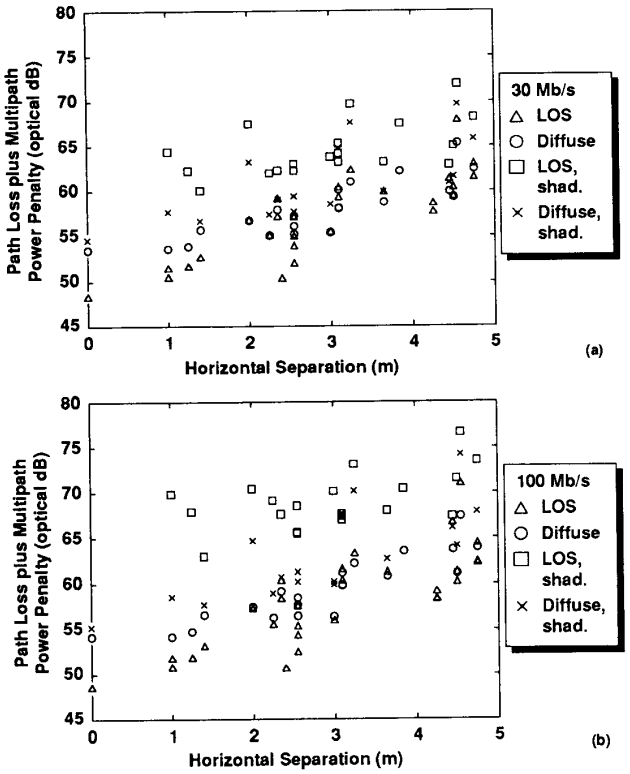

Fig. 12. Baseband on-off keying with zero-forcing decision-feedback equalization: path loss plus power penalty caused by intersymbol interference. Path losses are same as in Fig. 6, while power penalties are same as in Fig. 10.

scribed by a single-parameter model.

D. Combined Path Loss and ISI Penalty

For purposes of calculating the power budget of baseband OOK links operating over experimentally characterized channels, it is necessary to consider the combined effect of path loss and multipath power penalty. Fig. 12 presents the path loss plus power penalty for links using ZF-DFE at bit rates of 30 and 100 Mb/s. For links operating at 10 Mb/s, where multipath penalties are small, the corresponding quantity can be estimated conservatively by adding 1 dB to the path losses shown in Fig. 6.

VI. SUMMARY

Non-directed indoor infrared channels using intensity modulation and direct detection are described by an impulse response, or by a corresponding frequency response, which are fixed for a given configuration of transmitter, receiver and objects within the room. We have experimentally characterized the frequency response of such channels over the range from near-d.c. to 300 MHz, investigating LOS and diffuse link configurations, both with and without shadowing. We have computed channel impulse responses, path losses, and r.m.s. delay spreads. Channel impulse responses have been used to calculate multipath power penalties in on-off-keyed links operating at 10, 30 and 100 Mb/s, both without equalization and with zero-forcing decision-feedback equalization. We have found that unshadowed LOS configurations generally have smaller path losses, r.m.s. delay spreads and power penalties than their unshadowed diffuse counterparts. Shadowed LOS configurations, however, generally exhibit larger values of all three parameters than the corresponding shadowed diffuse configurations. For channels having small-to-moderate values of delay spread, we have found a strong correspondence between channel r.m.s. delay spreads and multipath power penalties with or without equalization.

VII. ACKNOWLEDGMENTS

The authors are grateful for informative discussions with M. D. Audeh, J. R. Barry, R Gharpurey, K. P. Ho and G. W. Marsh.

APPENDIX

DERIVATION OF CHANNEL MODEL

The purpose of this appendix is to show that in a non-directed infrared link using IM/DD, the total received photocurrent $Y(t)$ is related to the total transmitted optical power $X(t)$ by (1). To simplify the derivation, we neglect the noise term in (1), and we consider a flat detector lying in the x-y plane (see Fig. 13). At detector position (x, y), the total incident electric field $\vec{E}(x, y)$ can be written as the

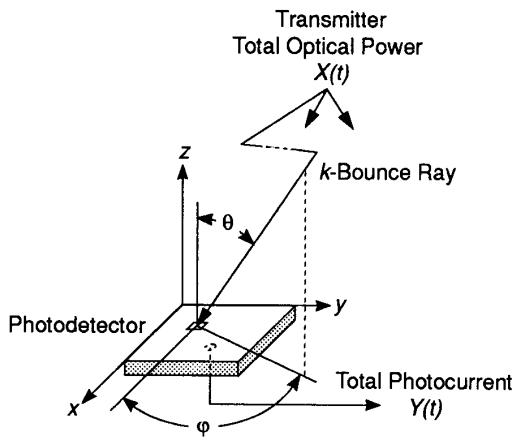

Fig. 13. Geometry used in derivation of channel model.

superposition of electric-field components arriving along direction (θ, φ) after undergoing k bounces en route from the source, denoted here by $\vec{e}(x, y, \theta, \varphi)$:

$$\vec{E}(x, y) = \sum_{k=0}^{\infty} \int_{2\pi} d\Omega \vec{e}(x, y, \theta, \varphi). \quad \text{(A.1)}$$

The integration is performed over the entire solid angle above the detector. Assuming that the transmitted signal is narrowband, we can express the electric-field components as:

$$\vec{e}(x, y, \theta, \varphi) = \vec{\alpha}_k(x, y, \theta, \varphi) \times \sqrt{X(t - \tau_k(x, y, \theta, \varphi))} e^{j[\Psi_0(t) + \Psi_k(x, y, \theta, \varphi)]}. \quad \text{(A.2)}$$

Here, $\vec{\alpha}_k(x, y, \theta, \varphi)$, assumed to be real, describes the magnitude and polarization of the field component arriving along direction (θ, φ) after undergoing k bounces; all attenuation along the propagation path or within the receiver collection optics is described by this parameter. The quantity $\tau_k(x, y, \theta, \varphi)$ describes the group delay of the IM envelope. The phase factor includes the propagation phase $\Psi_k(x, y, \theta, \varphi)$ in addition to a path-independent carrier phase $\Psi_0(t)$.

Neglecting shot noise, the total photocurrent is given by:

$$Y(t) = \frac{c\epsilon_0 R}{2} \int_{detector} dA |\vec{E}(x, y)|^2, \quad \text{(A.3)}$$

where R is the detector responsivity and the integral is over the detector surface. We make the simplifying assumptions that $\vec{\alpha}_k(x, y, \theta, \varphi) \approx \vec{\alpha}_k(\theta, \varphi)$ and $\tau_k(x, y, \theta, \varphi) \approx \tau_k(\theta, \varphi)$, i.e., along a given path the attenuation and delay are the same to all points on the detector surface; clearly the same is not true of the propagation phase. The total photocurrent becomes:

$$Y(t) = \frac{c\epsilon_0 R}{2} \sum_{k=0}^{\infty} \sum_{k'=0}^{\infty} \left[\int_{detector} dA e^{j[\Psi_k(x, y, \theta, \varphi) - \Psi_{k'}(x, y, \theta', \varphi')]} \times \int_{2\pi} d\Omega \int_{2\pi} d\Omega' \vec{\alpha}_k(\theta, \varphi) \vec{\alpha}_{k'}(\theta', \varphi') \sqrt{X(t - \tau_k(\theta, \varphi))} \times \sqrt{X(t - \tau_{k'}(\theta', \varphi'))} \right]. \quad \text{(A.4)}$$

Examining the integral in (A.4) that is taken over the detector surface, we note that when $k \neq k'$ or (θ, φ) differs even slightly from (θ', φ'), the phase term $[\Psi_k(x, y, \theta, \varphi) - \Psi_{k'}(x, y, \theta', \varphi')]$ undergoes changes of the order of 2π radians as x or y change by a distance of the order of the wavelength and the integral vanishes, since it is taken over a region whose dimensions are much larger than the wavelength. When $k = k'$ and $(\theta, \varphi) = (\theta', \varphi')$, the integral takes on a value equal to the detector surface area A_R. Hence this integral can be expressed approximately as:

$$\int_{detector} dA e^{j[\Psi_k(x, y, \theta, \varphi) - \Psi_{k'}(x, y, \theta', \varphi')]} \approx A_R \delta_{kk'} \delta(cos\theta - cos\theta') \delta(\varphi - \varphi'), \quad \text{(A.5)}$$

where δ_{mn} is the Kronecker delta and $\delta(x)$ is the Dirac delta function. With the substitution of (A.5) in (A.4), we can integrate the latter equation over Ω' and sum it over k' to obtain:

$$Y(t) = \frac{c\epsilon_0 A_R R}{2} \sum_{k=0}^{\infty} \int_{2\pi} d\Omega |\vec{\alpha}_k(\theta, \varphi)|^2 X(t - \tau_k(\theta, \varphi)). \quad \text{(A.6)}$$

Expression (A.6) can be rewritten as:

$$Y(t) = X(t) \otimes h(t), \quad \text{(A.7)}$$

where

$$h(t) = \frac{c\epsilon_0 A_R R}{2} \sum_{k=0}^{\infty} \int_{2\pi} d\Omega |\vec{\alpha}_k(\theta, \varphi)|^2 \delta(t - \tau_k(\theta, \varphi)). \quad \text{(A.8)}$$

We see that the impulse response (A.8) can be viewed as a sum of separate impulse responses $h^{(k)}(t)$, each describing the contribution from light that has undergone exactly k reflections en route from the source [7]. Each k-bounce impulse response $h^{(k)}(t)$ is a collection of unit impulses arriving from direction (θ, φ), retarded by the propagation delay $\tau_k(\theta, \varphi)$ and scaled by the power attenuation factor $|\vec{\alpha}_k(\theta, \varphi)|^2$. We note that these two quantities depend only on the macroscopic features of the propagation paths. When the propagation path lengths are changed on the order of a wavelength, there are no observable changes in $\tau_k(\theta, \varphi)$ and $|\vec{\alpha}_k(\theta, \varphi)|^2$. Thus, there is no measurable change in the channel impulse response, i.e., no "multipath fading".

References

[1] F. R. Gfeller and U. H. Bapst, "Wireless in-house data communication via diffuse infrared radiation", *Proceedings of the IEEE*, vol. 67, pp. 1474-1486, Nov. 1979.

[2] M. D. Kotzin, "Short-range communications using diffusely scattered infrared radiation", PhD Dissertation, Northwestern University: Evanston, IL, June 1981.
[3] M. D. Kotzin and A. P. van den Heuvel, "A duplex infra-red system for in-building communications," *IEEE Vehicular Technology Conference Proceedings*, pp. 179-185, 1986.
[4] J. M. Kahn, J. R. Barry, M. D. Audeh, J. B. Carruthers, W. J. Krause, and G. W. Marsh, "Non-directed infrared links for high-capacity wireless LANs", *IEEE Pers. Commun. Mag.*, vol. 1, no. 2, pp. 12-25, 1994.
[5] J. R. Barry, *Wireless Infrared Communications*. Boston: Kluwer Academic Publishers, 1994.
[6] E. A. Lee and D. G. Messerschmitt, *Digital Communications*, Second Edition. Boston: Kluwer Academic Publishers, 1994.
[7] J. R. Barry, J. M. Kahn, W. J. Krause, E. A. Lee, and D. G. Messerschmitt, "Simulation of multipath impulse response for wireless optical channels", *IEEE J. Sel. Areas of Comm.*, vol. 11, no. 3, pp. 367-379, Apr. 1993.
[8] J. D. Parsons, *The Mobile Radio Propagation Channel*. New York: Halsted Press, 1992.
[9] S. U. H. Qureshi, "Adaptive equalization," Ch. 12 of *Advanced Digital Communications* by K. Feher. Englewood Cliffs, NJ: Prentice-Hall, 1987.
[10] M. D. Audeh and J. M. Kahn, "Performance evaluation of baseband OOK for wireless indoor infrared LANs operating at 100 Mb/s", to be published in *IEEE Transactions on Communications*.
[11] M. D. Audeh, "Performance evaluation of baseband OOK for wireless indoor infrared LANs operating at 100 Mb/s", M.S. Report, University of California at Berkeley, Nov. 1992.

Joseph M. Kahn is Associate Professor in the Department of Electrical Engineering and Computer Sciences at UC Berkeley. He received the AB Physics (1981), MA Physics (1983), and PhD Physics (1986) from UC Berkeley. His PhD thesis was entitled "Hydrogen-Related Acceptor Complexes in Germanium". From 1987-90 he was a Member of Technical Staff in the Lightwave Communications Research Department of AT&T Bell Laboratories at Crawford Hill Laboratory in Holmdel, NJ, where he performed research on multi-gigabit-per-second coherent optical fiber transmission systems and related device and subsystem technologies. He demonstrated the first BPSK-homodyne optical fiber transmission system, and achieved world records for receiver sensitivity in multi-gigabit-per-second systems. He joined the faculty of UC Berkeley in 1990, where his research interests include optical fiber communication networks and transmission systems, local-area networks using free-space optical links, and optical interconnects in digital systems. Dr. Kahn is a recipient of the National Science Foundation Presidential Young Investigator Award, and is a member of the IEEE Communications Society and IEEE Lasers and Electro-Optics Society. He is serving currently as a Technical Editor of IEEE Personal Communications Magazine.

William J. Krause received a B.S. in electrical engineering from Johns Hopkins University, in 1990. In 1992 he received an M.S. in electrical engineering from U.C. Berkeley. His M.S. research involved wideband characterization of multipath free-space infrared channels. He is a member of Eta Kappa Nu and Tau Beta Pi.

Jeffrey B. Carruthers received the B.Eng. degree in computer systems engineering from Carleton University, Ottawa, Canada, in 1990, and joined Bell-Northern Research in Ottawa, working on development of SONET products until 1991. In 1993 he received the M.S. degree in electrical engineering from the University of California at Berkeley, where he is working toward the Ph.D. degree also in electrical engineering. His research interests are in broadband wireless communications. He is a member of the IEEE Communications, Vehicular Technology, and Social Implications of Technology Societies.